Journal of Catalysis 283 (2011) 34–44

Contents lists available at SciVerse ScienceDirect

Journal of Catalysis

journal homepage: www.elsevier.com/locate/jcat

Pd catalysts supported on $MnCeO_x$ mixed oxides and their catalytic application in solvent-free aerobic oxidation of benzyl alcohol: Support composition and structure sensitivity

Yuanting Chen [a], Huijian Zheng [a], Zhen Guo [a], Chunmei Zhou [a], Chuan Wang [b], Armando Borgna [b,*], Yanhui Yang [a,*]

[a] School of Chemical and Biomedical Engineering, Nanyang Technological University, Singapore 637459, Singapore
[b] Institute of Chemical and Engineering Sciences (ICES), A*STAR, 1 Pesek Road, Jurong Island, Singapore 627833, Singapore

ARTICLE INFO

Article history:
Received 10 May 2011
Revised 17 June 2011
Accepted 21 June 2011
Available online 31 August 2011

Keywords:
Manganese–cerium mixed oxides
Palladium
Benzyl alcohol oxidation
Composition and structure sensitivity

ABSTRACT

Both crystalline and amorphous $MnCeO_x$ supports were synthesized by co-precipitation and redox precipitation methods, respectively. Pd was subsequently deposited by an easy microwave-assisted polyol reduction procedure, leading to the formation of highly dispersed Pd nanoclusters. $MnCeO_x$ supports were remarkably enhanced in both catalytic activity and selectivity in the aerobic oxidation of benzyl alcohol, compared with pure MnO_x and CeO_2. The highest *q*TOFs (quasi-turnover frequencies) were achieved over Pd/7Mn3Ce-C (15,235 h^{-1}) and Pd/7Mn3Ce-A (14,438 h^{-1}), and the activity could be maintained over five consecutive reaction runs. Pd acts as a single active component, and the synergetic interactions among Pd, MnO_x, and CeO_2 result in enhanced catalytic activity. Good accessibility of the Pd active sites and a high surface concentration of Pd^0 contribute to the high initial reaction rate over crystalline $MnCeO_x$-supported Pd catalyst. Amorphous $MnCeO_x$-supported Pd catalyst exhibits enhanced catalyst stability due to mutual promotion between redox properties and oxygen mobility.

1. Introduction

Among various transition metal and rare earth mixed oxide catalysts, $MnCeO_x$ has attracted great attention because of its potential industrial applications, due to its high activity and versatility in many catalytic reactions, such as the catalytic wet oxidation of waste waters containing phenol [1], ammonia [2], and pyridine [3], the combustion of volatile organic compounds [4], and the conversion/decomposition of NO_x [5,6]. The superior activity of $MnCeO_x$ compared with pure MnO_x and CeO_2 oxides is attributed to the synergistic interactions between manganese and cerium oxides. The MnO_x domain, with high dispersion and multiple oxidation states, serves as the main active site, while CeO_2 acts as a promoter to enhance the oxygen mobility, due to its unique capacity of storing oxygen under oxidizing conditions and releasing oxygen under reducing conditions. This is achieved through the transformation between Ce^{4+} and Ce^{3+} oxidation states, forming abundant surface and bulk vacancies to improve the redox capabilities [7–9].

A large number of previous studies have demonstrated that the catalytic activity of $MnCeO_x$ composites strongly depends on the compositions and the textural, structural, and redox properties of these materials [1,10,11]. Several preparation routes have been developed to obtain $MnCeO_x$ with controlled physicochemical properties. Co-precipitation [12] and redox precipitation [7] are commonly employed to prepare crystalline and amorphous materials, respectively. The phase segregation of oxide domains correlates with the Mn/Ce molar ratio and the preparation method [13]. Due to the different precipitation kinetics of metal precursors, co-precipitation methods result in segregated manganese and cerium oxide crystallites with surface-enriched Ce. More specifically, either a thin layer of Ce-rich oxide covering the Mn crystallites or coexisting large MnO_x crystallites and small aggregates of Mn/Ce solid solution seems to be formed [14]. In contrast, redox precipitation routes favor the simultaneous precipitation of MnO_x and CeO_2, leading to a homogeneous mixture of Mn and Ce oxide species at the atomic level [15]. Our group has synthesized a series of amorphous $MnCeO_x$ catalysts by redox precipitation, which have been tested in the catalytic aerobic oxidation of benzyl alcohol [16]. This work demonstrated that MnO_x is the active component and the addition of highly dispersed CeO_2 promotes the catalytic performance by enhancing the redox properties of $MnCeO_x$.

Nonetheless, a rapid loss of catalytic activity was found over $MnCeO_x$ materials in most cases, which is mainly attributed to either the deposition of carbonaceous by-products on the catalyst surface or the leaching of the active metals during the reaction.

* Corresponding authors. Fax: +65 6794 7553.
E-mail addresses: armando_borgna@ices.a-star.edu.sg (A. Borgna), yhyang@ntu.edu.sg (Y. Yang).

0021-9517/$ - see front matter © 2011 Elsevier Inc. All rights reserved.
doi:10.1016/j.jcat.2011.06.021

This activity loss can be suppressed by adding a promoter. Santiago et al. reported that doping $MnCeO_x$ mixed oxides with a certain amount of potassium showed improved performance and stability of the catalyst, since K^+ could act as a modifier or chemical promoter [17]. Hamoudi et al. suggested that the catalyst deactivation could be diminished by a three-component catalyst using noble metals promoters, e.g., Ag and Pt, to significantly reduce the amount of carbonaceous deposits, prolonging the catalyst life [18]. Tang et al. studied the effect of Ag addition to $MnCeO_x$ on the complete oxidation of formaldehyde and suggested that the enhanced activity was due to improved oxygen activation on the catalyst surfaces and to oxygen mobility among Ag, Mn, and Ce [12]. Ru catalysts supported on $MnCeO_x$ were also reported to be highly active for alcohol oxidation reactions [19,20]. Recently, Zou et al. have shown that a Pd/MnO_x–CeO_2 catalyst synthesized by a surfactant-assisted precipitation method exhibits excellent activity in CO oxidation due to accelerated oxygen activation in the gas phase and oxygen transfer via spillover [21].

In this study, we prepared both crystalline and amorphous $MnCeO_x$ supports. Then, Pd particles were supported on these mixed oxides by an easy microwave-assisted polyol reduction (MAPR) method. The catalytic performance in the selective oxidation of benzyl alcohol using molecular oxygen under solvent-free conditions was evaluated. Benzyl alcohol oxidation was selected as a probe reaction due not only to its relatively high reactivity but also to the limited number of possible by-products. Various physicochemical characterization techniques were employed to investigate the textural, structural, and redox properties as well as the surface composition of these $Pd/MnCeO_x$ catalysts. The catalytic performance was correlated with these properties in a comparative manner between amorphous and crystalline support materials.

2. Experimental

2.1. Catalyst synthesis

Crystalline $MnCeO_x$ supports with different Mn/Ce molar ratios (1:3, 7:3, and 10:1) were synthesized following a well-established co-precipitation procedure [8]: 100 mL of a solution of $Mn(NO_3)_2{\cdot}4H_2O$ and $Ce(NO_3)_3{\cdot}6H_2O$ with a total concentration of 150 g/L and a given nominal Mn/Ce mole ratio was prepared. A 2-M NaOH aqueous solution was added dropwise at 50 °C under vigorous stirring until pH 10.5. The precipitate was further aged at 50 °C for 2 h. The obtained solid was filtered, washed with deionized water, dried at 100 °C for 12 h, and calcined at 500 °C for 6 h in air. The as-calcined $MnCeO_x$ support was designed as *x*Mn*y*Ce-C, *x*/*y* being the nominal molar ratio of Mn/Ce. The amorphous $MnCeO_x$ supports were prepared by redox precipitation [15]: A certain amount of $KMnO_4$ precursor dissolved in deionized water was titrated with an aqueous solution containing both $Mn(NO_3)_2{\cdot}4H_2O$ and $Ce(NO_3)_3{\cdot}6H_2O$ at 70 °C under vigorous stirring, where $KMnO_4$ was in 10% stoichiometric excess. A 2-M NaOH aqueous solution was added dropwise to maintain a constant pH value at 8.0. After further stirring for 1 h, the obtained solid was filtered, repeatedly washed with hot deionized water, dried at 100 °C for 12 h, and calcined in air at 400 °C for 6 h. This support was denoted as *x*Mn*y*Ce-A. For comparison, pure manganese oxide (MnO_x) and cerium oxide (CeO_2) were also prepared by co-precipitation using $Mn(NO_3)_2{\cdot}4H_2O$ and $Ce(NO_3)_3{\cdot}6H_2O$ as precursors.

Palladium nanoparticles supported on these calcined $MnCeO_x$ mixed oxides were successfully prepared by an easy MAPR procedure as reported by Guo et al. [22]. To deposit Pd precursors onto $MnCeO_x$ mixed oxides, 0.1 g of support was immersed in 94.0 μL of $PdCl_2$ aqueous solution (0.05 M) and dried at 100 °C in vacuum. The obtained solid was added to ethylene glycol (40 mL) and sonicated for 30 min to produce a homogenous suspension. The suspension was transferred into a three-necked flask with a condenser and placed in a microwave reactor (Sineo, MAS-II). The slurry was agitated by a magnetic stirrer, and the temperature inside the flask was monitored by an infrared sensor. The suspension was heated to 160 °C in 0.5 min and kept at the same temperature for another 1.5 min. After cooling to room temperature, the solid was filtered, washed with deionized water, and dried at 100 °C in vacuum. The as-synthesized catalyst was denoted as Pd/*x*Mn*y*Ce-M (M = C or A for crystalline or amorphous structure, respectively).

2.2. Catalyst characterizations

Nitrogen physisorption isotherms were measured at −196 °C on a static volumetric instrument (Autosorb-6b, Quanta Chrome). Prior to each measurement, the sample was degassed at 250 °C for 12 h under high vacuum. The specific surface area was calculated by the Brunauer–Emmett–Teller method [23]; the pore size distribution was calculated by the Barrett–Joyner–Halenda method using the desorption branch [24].

Powder X-ray diffraction (XRD) patterns were recorded on a Bruker AXS D8 diffractometer under ambient conditions using filtered Cu Kα radiation (λ = 1.5406 Å) operated at 40 kV and 40 mA. Diffraction data were collected from 20° to 70° with a resolution of 0.02° (2θ). Prior to the test, samples were dried at 100 °C overnight. The average crystallite sizes of $MnCeO_x$ grains were calculated from the full width at half maximum of the ceria (1 1 1) or Mn_2O_3 (Bixbyite-C) (2 2 2) peak according to Scherrer's equation and using a Scherrer constant of 0.89. The lattice constants were derived following the Cohen procedures [25].

Transmission electron microscopy (TEM) was performed on a JEOL JEM-2100F operated at 200 kV. The samples were suspended in ethanol and dispersed on a holey carbon-coated Cu grid. The metal content was measured by inductively coupled plasma (ICP) analysis using a dual-view Optima 5300 DV ICP-OES system. Nitric acid was used to dissolve the sample.

Hydrogen temperature-programmed reduction (H_2 TPR) and oxygen temperature-programmed desorption (O_2 TPD) measurements were carried out using an Autosorb-1C system (Quanta Chrome), equipped with a thermal conductivity detector. Prior to each H_2 TPR run, 100 mg of the sample was loaded in the quartz tube and pretreated with ultra-pure air at 100 °C for 3 h. After cooling to room temperature, the gas flow was switched to 5 vol.% H_2/Ar and the baseline was monitored until it became stable. The sample cell was heated at a ramping rate of 5 °C/min and held at 600 °C for 1 h to ensure complete reduction. For the O_2 TPD test, 100 mg of the sample was pretreated in pure O_2 at 550 °C for 1 h. After cooling to room temperature, the sample was flushed with pure helium until the baseline became stable. The desorption was conducted by heating the sample to 900 °C with a heating rate of 10 °C/min.

X-ray photoelectron spectroscopy (XPS) was performed on a VG Escalab 250 spectrometer equipped with an Al anode (Al Kα = 1486.6 eV). The background pressure in the analysis chamber was lower than 1×10^{-7} Pa. Measurements were performed using 20-eV pass energy, 0.1-eV step, and 0.15-min dwelling time. The correction of the binding energies (BE) was carried out using the C1*s* peak of adventitious C at 284.6 eV. The background contribution *B* (E) caused by inelastic process was obtained by the Shirley method and subtracted. The curve fitting was performed with a Gaussian–Lorentzian shape function to deconvolute the overlapping peaks. The atomic ratios of the different elements were estimated using the ratio of the normalized peak intensities corrected with the atomic sensitivity factors (7.399 for Ce 3*d*, 2.420 for Mn 2*p*, 0.711 for O 1*s*, and 4.462 for Pd 3*d*).

2.3. Catalytic activity

The solvent-free aerobic oxidation of benzyl alcohol using molecular O_2 was carried out in a batch-type reactor operated under atmospheric conditions. Experiments were conducted using a three-necked glass flask (capacity 25 mL) precharged with 5.4 g of benzyl alcohol and 20 mg of catalyst. The mixture was stirred using a magnetic stirrer and heated in a silicon oil bath. The system was equipped with a thermocouple to control the temperature and a reflux condenser. In each reaction run, the mixture was heated to 160 °C under vigorous stirring (stirring rate 1000 rpm). Oxygen was bubbled into the mixture at a constant flow rate of 20 mL/min using a mass flow controller to initiate the reaction. After the allowed reaction time, the catalyst powder was filtered off and the liquid organic products were analyzed using an Agilent 6890 gas chromatograph equipped with an HP-5 capillary column (30 m long and 0.32 mm in diameter, packed with silica-based Supel-cosil). Dodecane was used as the internal standard to calculate benzyl alcohol conversion and benzaldehyde selectivity. The conversion, selectivity, and *quasi*-turnover frequency (*q*TOF) are defined as follows:

$$\text{conversion}/\% = \frac{\text{moles of reactant converted}}{\text{moles of reactant in feed}} \times 100\%$$

$$\text{selectivity } (\%) = \frac{\text{moles of product formed}}{\text{moles of reactant converted}} \times 100\%$$

$$q\text{TOF } (\text{h}^{-1}) = \frac{\text{moles of reactant converted}}{\text{moles of total active sites} \times \text{reaction time}}.$$

3. Results and discussion

3.1. Catalytic results

Both crystalline and amorphous $MnCeO_x$-supported Pd catalysts have been tested in the selective oxidation of benzyl alcohol in the presence of molecular oxygen. The results are listed in Table 1. It is possible to deposit 0.5 wt.% Pd on MnO_x support, but only 0.36 wt.% on CeO_2 In addition, the Pd loading increases with the addition of Mn to Ce. Therefore, mixing Mn with Ce to form $MnCeO_x$ mixed oxides leads to an enhanced Pd deposition, resulting in more catalytic active sites. Despite a 23.4% conversion of benzyl alcohol, Pd/CeO_2 shows 88.9% selectivity toward benzaldehyde due to the formation of a large amount of toluene as an undesired by-product. Pd/MnO_x exhibits a poor catalytic conversion of 17.9% along with 99.4% benzaldehyde selectivity. Regardless of the support structure and composition, either benzyl alcohol conversion or selectivity toward benzaldehyde can be enhanced using $MnCeO_x$ mixed oxide supports. The benzaldehyde selectivity is well maintained above 98%, whereas the catalytic activity depends on the nature and composition of support materials. For Pd catalysts supported on both $MnCeO_x$-C and $MnCeO_x$-A materials, the catalytic activity (*q*TOF) first increases to a maximum value after the addition of a small amount of Mn to Ce, and then slightly decreases with further addition. The highest *q*TOFs are achieved over Pd/7Mn3Ce-C (15,325 h^{-1}) and Pd/7Mn3Ce-A (14,438 h^{-1}) for $MnCeO_x$ crystalline and amorphous support materials, respectively. A control reaction was also carried out over a physical mixture of Pd/CeO_2 and Pd/MnO_x catalysts. A poor conversion of 9.6% is obtained, indicating that only chemically mixed Mn and Ce species can facilitate the catalytic reaction. In addition, bare supports show negligible catalytic activity (entries 10 and 11), implying that Pd acts as the sole active species. Therefore, the improved catalytic activity on Mn–Ce mixed oxides could be correlated with the synergetic interactions among Pd, CeO_2, and MnO_x domains. As a structural and electronic promoter, CeO_2 improves the oxygen storage and release ability, enhances the oxygen mobility and availability, and tunes the redox properties of the mixed oxides when associated with MnO_x [16].

The evolution of the catalytic performance as a function of time was studied over Pd/7Mn3Ce-C and Pd/7Mn3Ce-A catalysts. The results are depicted in Fig. 1. The conversion of benzyl alcohol increases monotonically with the reaction time, whereas the *q*TOF decreases. The selectivity toward benzaldehyde is high ($\geqslant$97%) over both catalysts during the first 0.5 h of reaction. Nevertheless, it gradually deteriorates at longer reaction times, which is ascribed to the formation of benzoic acid by further oxidation of benzaldehyde. The benzyl alcohol conversion over Pd/7Mn3Ce-C reaches a plateau after 4 h, while that of Pd/7Mn3Ce-A increases continuously, implying faster deactivation for Pd/7Mn3Ce-C, which may be attributed to the pronounced deposition of carbonaceous species [19]. After 12 h, 63.1% and 81.9% conversion of benzyl alcohol is obtained over Pd/7Mn3Ce-C and Pd/7Mn3Ce-A catalysts, respectively.

Recyclability is a critical factor in evaluating a heterogeneous catalyst. When the metal component is not properly anchored onto the support, it may be leached out during the course of the reaction, resulting in an active homogeneous catalyst and a loss of catalytic activity on subsequent runs. The recyclabilities of both

Table 1
Catalytic performance of 0.5 wt.% Pd-containing catalysts supported on $MnCeO_x$.[a]

Entry	Catalyst	Pd content[b] (wt.%)	Conversion (%)	Selectivity (%)			*q*TOF[c] (h^{-1})
				Benzaldehyde	Toluene	Benzoic acid	
1	Pd/CeO_2	0.36	23.4	88.9	11.1	0	17,572
2	Pd/1Mn3Ce-C	0.28	15.6	99.1	0.9	0	14,850
3	Pd/7Mn3Ce-C	0.32	18.4	98.6	0.4	0	15,325
4	Pd/10Mn1Ce-C	0.41	23.2	98.7	0.8	0.5	15,066
5	Pd/1Mn3Ce-A	0.27	12.3	98.3	1.2	0.4	12,085
6	Pd/7Mn3Ce-A	0.38	20.6	99.3	0.7	0	14,438
7	Pd/10Mn1Ce-A	0.51	15.6	99.0	1.0	0	8688
8	Pd/MnO_x	0.5	17.9	99.4	0.6	0	9526
9	Pd/CeO_2 + Pd/MnO_x[d]	0.41	9.6	100	0	0	6246
10	10Mn1Ce-C	–	1.0	100	0	0	–
11	7Mn3Ce-A	–	0.9	100	0	0	–
12	Pd/7Mn3Ce-C[e]	0.32	0.9	97.9	2.1	0	777
13	Pd/7Mn3Ce-A[e]	0.38	0.9	99	1	0	605

[a] Reaction conditions: catalyst, 20 mg; benzyl alcohol, 50 mmol; O_2, 20 mL/min; temperature, 160 °C; reaction time, 1 h; carbon balance, 98.5%.
[b] Pd content was tested by ICP.
[c] *q*TOF is calculated using the Pd content obtained from ICP.
[d] Physical mixture of Pd/CeO_2 and Pd/MnO_x catalyst (1:1 mass ratio).
[e] N_2 used instead of O_2.

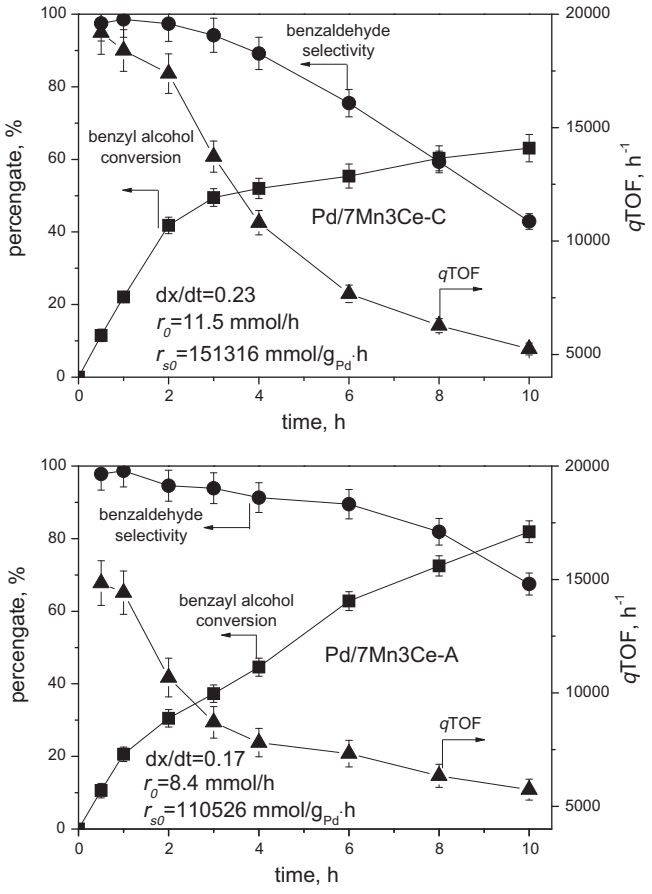

Fig. 1. Time courses of Pd/7Mn3Ce-C and Pd/7Mn3Ce-A for benzyl alcohol oxidation. Reaction conditions: catalyst, 20 mg; benzyl alcohol, 50 mmol; O_2, 20 mL/min; temperature, 160 °C; reaction time, 1 h.

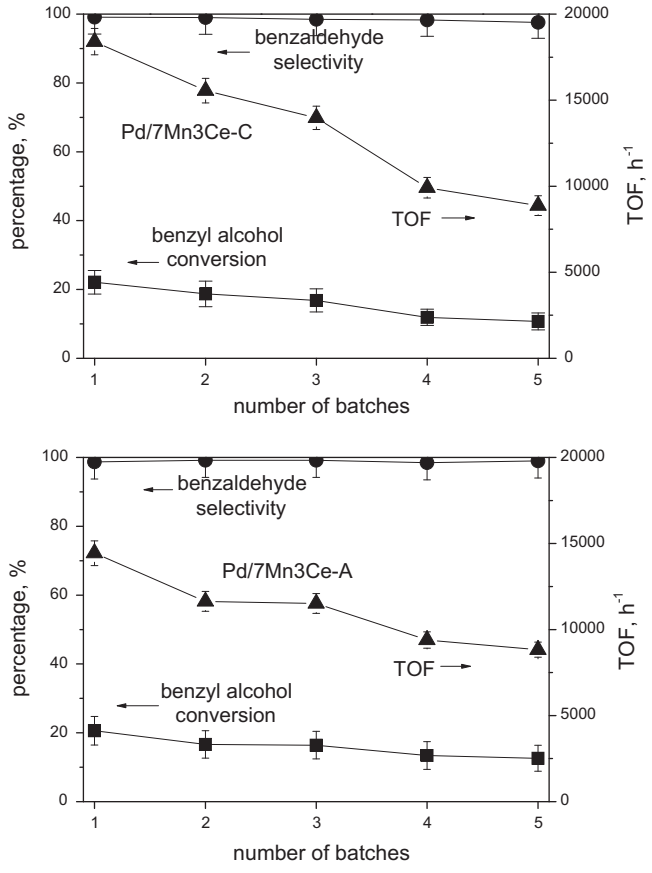

Fig. 2. Recyclability of Pd/7Mn3Ce-C and Pd/7Mn3Ce-A for benzyl alcohol oxidation. Reaction conditions: catalyst, 20 mg; benzyl alcohol, 50 mmol; O_2, 20 mL/min; temperature, 160 °C; reaction time, 1 h.

Pd/7Mn3Ce-C and Pd/7Mn3Ce-A were examined for five consecutive cycles, and the results are depicted in Fig. 2. The catalyst was recovered after each reaction run, thoroughly washed with acetone, dried at 60 °C, and reused in the next reaction. Both catalysts maintain the high benzaldehyde selectivity well and undergo a moderate decrease in the catalytic activities, which could be attributed to the loss of catalyst during the recovery. The Pd content after five consecutive reaction cycles was almost the same as that of the fresh catalysts. This clearly suggests that the interaction between Mn and Ce, forming either crystalline or amorphous $MnCeO_x$ mixed oxides, not only improves the catalytic performance but also enhances the catalyst stability.

3.2. Catalyst characterizations

Table 2 summarizes the textural properties of all synthesized $MnCeO_x$ support materials, as well as MnO_x and CeO_2. Crystalline MnO_x has a rather low surface area of 36.3 m^2/g. The specific surface area increases to 48.0 m^2/g upon addition of Ce and monotonically increases with further Ce addition. 1Mn3Ce-C shows a specific surface area of 116.0 m^2/g, which is higher than that of CeO_2. The increased surface area after addition of Ce to MnO_x implies close interaction between MnO_x and CeO_2. Similarly, an increase in Ce content also gradually increases the surface area for $MnCeO_x$-A samples, the 1Mn3Ce-A sample being the one that possesses the largest surface area (217.6 m^2/g). In general, the pore volumes of all $MnCeO_x$ samples are larger than those of pure MnO_x and CeO_2. Amorphous $MnCeO_x$ support materials exhibit larger surface areas but smaller pore diameters than crystalline $MnCeO_x$ samples, implying that the crystal growth of $MnCeO_x$-C can be suppressed more significantly during the redox reaction among Mn^{2+}, Ce^{3+}, and MnO_4^- [26].

Fig. 3 shows the XRD patterns of $MnCeO_x$ supports along with the catalysts containing 0.5 wt.% Pd. The calculated average grain sizes of CeO_2 and MnO_x and the lattice constants (only for crystalline samples) are listed in Table 2. Pure MnO_x exhibits the characteristic diffraction peaks ascribed to Mn_2O_3 (Bixbyite-C, PDF# 41-1442) and Mn_3O_4 (Hausmannite, PDF# 24-0734), suggesting the coexistence of +2 and +3 oxidation states of Mn. The XRD pattern of pure cerium oxide shows intense and sharp peaks at 2θ = 28.5°, 33.1°, 47.5°, and 56.3°, which can be assigned to CeO_2 (PDF# 43-1002). For the 1Mn3Ce-C sample, no other crystalline phases, but broad reflections due to the cubic fluorite structure of CeO_2, are observed, which could be attributed to the formation of a solid solution between manganese and cerium oxides by incorporation of Mn cations into CeO_2 lattices. For 7Mn3Ce-C and 10Mn1Ce-C samples, in addition to the broad reflection peaks of CeO_2, diffraction peaks ascribed to Mn_2O_3 and Mn_3O_4 appear, suggesting the coexistence of segregated Mn and Ce oxide phases. The remarkable weakening and broadening of these diffraction peaks with increasing Ce content suggest that the incorporated cerium enhances the dispersion for both Ce and Mn species [27]. Furthermore, several weak diffraction peaks that fit the *d*-spacing of MnO_2 (Ramsdellite, PDF# 39-0375) and Mn_5O_8 (PDF# 39-1218) are also observed, implying that Ce addition might increase the oxidation state of Mn and stabilize Mn oxide species in higher oxidation states. These results are consistent with a recent report indicating that the phase composition of crystalline $MnCeO_x$ strongly depends on the molar ratio of Mn/Ce [28].

Table 2
Textural and structural properties of $MnCeO_x$ support materials with different Mn/Ce molar ratios.

Entry	Sample	Molar ratio (Mn/Ce)	Surface area (m^2/g)	Pore volume (cm^3/g)	Pore diameter (nm)	Grain size (nm)	Lattice constant (nm)
1	CeO_2	0:1	79.4	0.19	9.1	13.3	0.5416[a]
2	1Mn3Ce-C	1:3	116.0	0.32	13.4	5.0	0.5279[a]
3	7Mn3Ce-C	7:3	67.6	0.38	15.7	5.3	0.5318[a]
4	10Mn1Ce-C	10:1	48.0	0.36	24.9	8.4	0.5376[a]
5	1Mn3Ce-A	1:3	217.6	0.46	9.0	–	–
6	7Mn3Ce-A	7:3	190.6	0.47	1.8	–	–
7	10Mn1Ce-A	10:1	101.5	0.32	3.6	–	–
8	MnO_x	1:0	36.3	0.33	36.4	38.3	0.9362[b]

[a] Grain size and lattice constant were calculated according to the CeO_2 (1 1 1) peak.
[b] Grain size and lattice constant were calculated according to the Mn_2O_3 (Bixbyite-C) (2 2 2) peak.

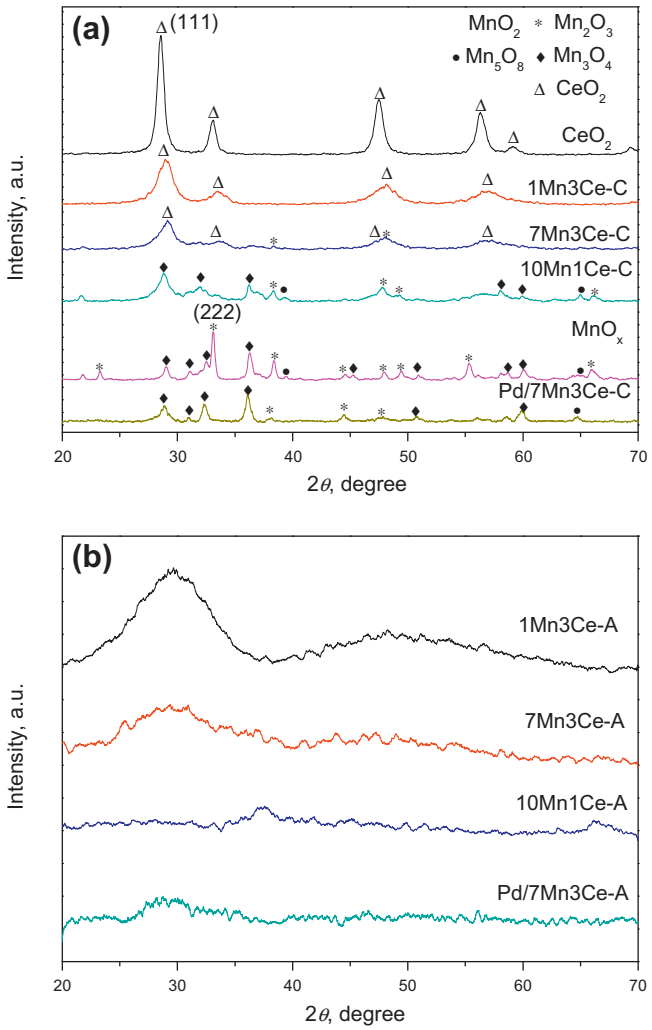

Fig. 3. XRD patterns of $MnCeO_x$ supports and of catalysts containing 0.5 wt.% Pd: (a) crystalline; (b) amorphous.

Notably, the diffraction peaks attributed to the fluorite-like structure of CeO_2 shift toward higher Bragg angles in the presence of more Mn, implying the contraction of the CeO_2 unit cell. This is further confirmed by the changes in lattice constants of $MnCeO_x$-C samples, as depicted in Table 2. All the calculated lattice constants monotonically increase with increasing Mn content. Nevertheless, all constants are smaller than those of both pure CeO_2 (0.5146 nm) and MnO_x (0.9362 nm). Considering the smaller ionic radius of Mn^{2+} (0.065 nm) and Mn^{3+} (0.066 nm) than of Ce^{4+} (0.094 nm), the small lattice constants for $MnCeO_x$-C suggest that Mn ions may be incorporated into the ceria lattice, provoking the unit cell contraction. This suggests the formation of manganese–cerium oxides solid solutions. Furthermore, the diffraction peaks of CeO_2 broaden after Mn addition, indicating that crystal growth and concomitant sintering are suppressed. Thus, small crystallites with a more defective lattice and less crystalline character are formed.

Amorphous $MnCeO_x$-A samples exhibit significantly different XRD patterns than $MnCeO_x$-C. A broad peak spanned in the 2θ range of 20–38°, along with other less intense peaks in the range of 40–60°, suggests the lack of long-range order, which may be due to the hindered growth of large crystalline domains during redox precipitation, since Mn and Ce are intimately contacted [26]. A decrease of peak intensity with increasing Mn/Ce ratio implies that these diffractions are mainly associated with ceria species [15]. No reflections due to Pd can be observed after Pd deposition on either 7Mn3Ce-C and 7Mn3Ce-A supports, indicating the highly dispersed nature of these supported Pd nanoparticles.

Fig. 4 shows TEM images of Pd/7Mn3Ce-C and Pd/7Mn3Ce-A, as well as Pd/CeO_2 and Pd/MnO_x. All these catalysts, except amorphous Pd/7Mn3Ce-A, consist of a large number of nanocrystallites of metal oxide grains. According to size and morphology, two kinds of particles can be distinguished for Pd/MnO_x catalyst: round large and nonfaceted crystals with a size of ca. 40 nm and small aggregates (<7 nm), which are attributed to Mn_2O_3 and Mn_3O_4. For Pd/7Mn3Ce-C catalyst, a new crystal phase besides Mn_2O_3 and Mn_3O_4 can be discerned, which exhibits a rod-like shape with a length ranging from several nanometers to several micrometers. These nanorods were also observed by Perez-Omil et al. and attributed to MnO_2 [29]. Pd/7Mn3Ce-A exhibits only a densely packed amorphous matrix. The CeO_2 nanocrystallites are of ca. 15 and 8 nm for Pd/CeO_2 and Pd/7Mn3Ce-C, respectively, in good agreement with the grain sizes derived from XRD (listed in Table 2). This further confirms that adding a small amount of Ce not only increases the surface area of MnO_x but also enhances the dispersion for both Ce and Mn species [27]. Therefore, the Mn and Ce oxide phases in $Pd/MnCeO_x$-A are homogeneously mixed at the quasi-molecular level, forming a prevalently amorphous structure [13], whereas in the $Pd/MnCeO_x$-C sample, they mostly retain the typical features of MnO_x crystallites. Pd nanoclusters with small sizes and high dispersion can be seen on the support surfaces. On Pd/7Mn3Ce-A, only the sporadic presence of Pd nanoparticles is observed, implying that Pd species may be embedded in the irregular and amorphous matrix.

H_2 TPR profiles of representative $MnCeO_x$ support materials are illustrated in Fig. 5. Pure MnO_x shows two main reduction peaks (327 and 452 °C), which are ascribed to a two-step reduction: reduction of MnO_2 and/or Mn_2O_3 to Mn_3O_4 and subsequent reduction of Mn_3O_4 to MnO [30]. Pure CeO_2 shows a broad and indistinct reduction peak starting from 300 °C with a maximum at 380 °C, which is assigned to the easily reducible Ce^{4+} species [1,16]. When Mn is mixed with Ce to form crystalline 7Mn3Ce-C, the two-step Mn reduction is retained. However, the two characteristic reduction peaks shift to lower temperatures, 287 and 393 °C,

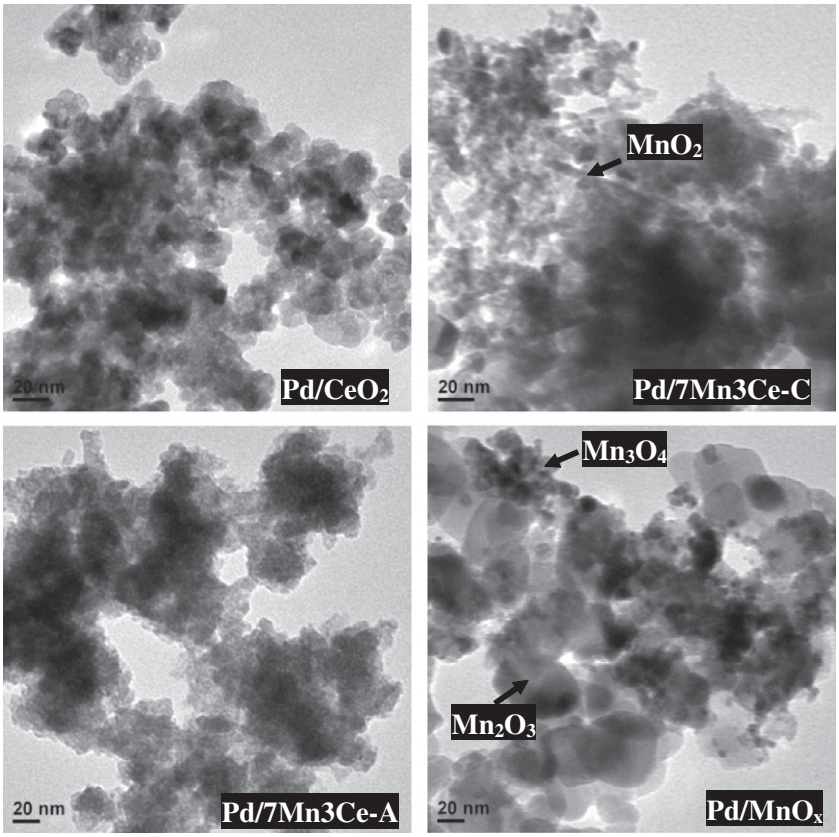

Fig. 4. TEM images of representative $MnCeO_x$-supported Pd catalysts.

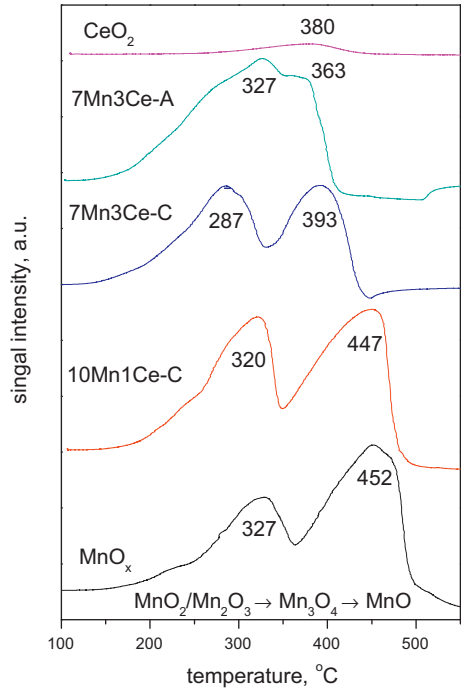

Fig. 5. H_2 TPR profiles of representative $MnCeO_x$ support materials.

respectively, indicating improved reducibility and oxygen mobility caused by the incorporation of Ce as well as the interaction between manganese and cerium oxides [1,12]. The increased ratio of first to second peak area for 10Mn1Ce-C compared with MnO_x qualitatively reveals the existence of a larger fraction of manganese oxide species having higher oxidation states. To study the possible effect of bulk Mn/Ce composition, the reducibility of 10Mn1Ce-C was also examined, as depicted in Fig. 5. The 10Mn1Ce-C sample gives a TPR profile similar to that of 7Mn3Ce-C, though both reduction peaks of Mn slightly shift to higher temperatures, further confirming the enhanced reducibility provided by incorporating Ce.

The reduction of amorphous 7Mn3Ce-A shows a different pattern, exhibiting two poorly resolved peaks at 327 and 363 °C, respectively. In fact, these two overlapped peaks can be assigned to the reduction of isolated Mn^{4+} [15] and Mn^{3+} species due to the absence of reduction at around 450 °C. The remarkable shift toward lower temperature is attributed to three factors: molecular-level Mn–Ce interdispersion, higher average oxidation states, and strong Mn–O–Ce interaction [13]. The reduction is promoted by highly coordinatively unsaturated Mn species and, perhaps, the presence of neighboring Ce^{4+} ions, which undergo reduction to Ce^{3+} species. The TPR results reveal that the mobility and availability of lattice oxygen are enhanced by the incorporation of Ce and the strong synergistic interaction between Mn and Ce oxides. CeO_2, well known for its oxygen storage capacity, can provide oxygen to Mn, thereby increasing its oxidation state. Manganese species possess higher oxidation states (+3 and +4) and enhanced reducibility in amorphous $MnCeO_x$ than those in crystalline counterpart (+2, +3, and +4).

TPD tests, an effective method to examine the mobility of oxygen species, were performed on three representative catalysts: Pd/7Mn3Ce-A, Pd/7Mn3Ce-C, and Pd/10Mn1Ce-C. The results are shown in Fig. 6. The indistinct and board peak at 260 °C is assigned to the surface-active oxygen species, probably chemisorbed oxygen O_2^-, which are originated from the oxygen vacancies on the interface of MnO_x and CeO_2 during the oxidation pretreatment before the TPD tests [21]. This peak is more intense in Pd/7Mn3Ce-A than in Pd/7Mn3Ce-C, indicating higher abundance of O_2^- component over

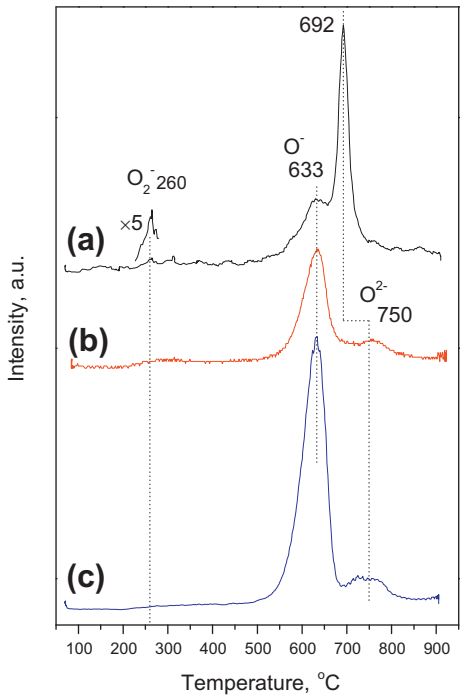

Fig. 6. O_2 TPD profiles of representative Pd/$MnCeO_x$ catalysts: (a) Pd/7Mn3Ce-A; (b) Pd/7Mn3Ce-C; (c) Pd/10Mn1Ce-C.

Pd/7Mn3Ce-A. Nonetheless, this peak nearly disappears in Pd/10Mn1Ce-C, implying the lack of such interface oxygen species, probably due to the decrease of the Mn–Ce interface as a result of discrete contact between large MnO_x and CeO_2 crystallites. The peak at ca. 630 °C, which is attributed to the chemisorbed atomic oxygen O^-, is significantly intense in Pd/7Mn3Ce-C and Pd/10Mn1Ce-C, while it becomes a shoulder in the Pd/7Mn3Ce-A. The board peak centered at 750 °C in both Pd/7Mn3Ce-C and Pd/10Mn1Ce-C samples is assigned to the lattice oxygen O^{2-}. However, this peak drastically shifts to 692 °C in Pd/7Mn3Ce-A sample, indicating remarkably enhanced oxygen mobility.

XPS is a useful technique for analyzing phenomena occurring at the outermost layers of $MnCeO_x$ surfaces and evaluating the surface species (Ce, Mn, O, and Pd) in nonstoichiometric surface oxides of both crystalline and amorphous $MnCeO_x$ supports and their corresponding Pd-containing catalysts. To understand the effect of support structure and Pd deposition on the surface chemistry, we have examined 7Mn3Ce-C and 7Mn3Ce-A supports and their corresponding Pd-containing catalysts. The evolution of XPS spectra of Ce3*d*, Mn2*p*, O1*s*, and Pd3*d* core levels are shown in Fig. 7, and the surface compositions are summarized in Table 3. 7Mn3Ce-A exhibits a Mn/Ce ratio (2.13) that is close to the theoretical bulk composition, indicating homogeneous dispersion of Mn and Ce species due to simultaneous co-precipitation, whereas 7Mn3Ce-C gives a slightly lower Mn/Ce atomic ratio (1.96), suggesting that the crystalline support is surface-enriched in Ce. This Ce surface enrichment of co-precipitated $MnCeO_x$ can be attributed either to partial coverage of Mn crystals by a thin layer of Ce-rich oxide or to the presence of large MnO_x crystals, which contribute less significantly to the total surface area than small Ce-rich Mn–Ce solid solution crystallites [14]. After Pd is added, the Mn/Ce ratio remains almost unchanged for Pd/7Mn3Ce-A (2.19), while it decreases for Pd/7Mn3Ce-C (1.73), implying that Pd is uniformly dispersed in Pd/7Mn3Ce-A while it exhibits preferential anchoring on Mn species in Pd/7Mn3Ce-C. In amorphous samples, the relative abundance of both Mn and Ce is higher than in crystalline samples, further verifying the good interdispersion of Mn and Ce species in amorphous $MnCeO_x$. Pd/7Mn3Ce-C shows a slightly higher surface Pd concentration (0.48%) than Pd/7Mn3Ce-A (0.31%), suggesting that more exposed Pd active sites are available on the Pd/7Mn3Ce-C sample, while Pd may be partially embedded or covered in Pd/7Mn3Ce-A. Trovarelli et al. also reported that precious metals such as Pt and Pd interact strongly with CeO_2 and tend to penetrate inside it [9].

The Ce3*d* core-level spectra in Fig. 7a were deconvoluted using two spin–orbit components (u and v refer to the $3d_{3/2}$ and $3d_{5/2}$ spin–orbit components, respectively) to distinguish Ce^{3+} and Ce^{4+} contributions. The spectra of Ce^{4+} can be resolved into six features (u, u'', u''', v, v'', and v'''), while Ce^{3+} can be fitted with two features (u' and v') [21]. The high-BE doublet u'''/v''' at 916.9 and 898.5 eV is assigned to the final state of $Ce^{4+}3d^94f^0\ O2p^6$. The doublet u''/v'' at 907.3 and 888.5 eV is attributed to the hybridization state of $Ce^{4+}3d^94f^1\ O2p^5$ and the doublets u/v at 901.6 and 883.0 eV correspond to the state of $Ce^{4+}3d^94f^2\ O2p^4$. The doublets u^o/v^o, which correspond to the $Ce^{3+}3d^04f^1\ O2p^6$ final state, are absent in all samples, indicating that +4 is the dominant oxidation state. The 7Mn3Ce-C support exhibits higher intensities of the doublets v'''/u''' and v''/u'' than the 7Mn3Ce-A sample even after Pd is added, suggesting the presence of more Ce^{4+} species in crystalline $MnCeO_x$ samples. The relative abundances of Ce^{4+} and Ce^{3+} are estimated based on the fitted peak areas of the XPS Ce3*d* spectra and are listed in Table 3. Despite the predominance of Ce^{4+}, Ce^{3+} can be detected in these samples. A higher abundance of Ce^{3+} exists in 7Mn3Ce-A than in 7Mn3Ce-C. Anchoring Pd onto the support may result in more Ce^{3+} species at the expense of Ce^{4+}, which is clearly suggested by the stronger u' and v' peaks. The existence of Ce^{3+} implies the formation of oxygen vacancies, since the creation of each Ce^{3+} generates two oxygen vacancies, while Ce^{3+} is assumed to retain the normal coordination number of 8, as in the case of Ce^{4+}. It was suggested that the perturbation of Ce–O and/or M–O bonds in CeO_2–MO_x mixed oxides would form highly disordered oxygen in the lattice, promoting oxygen transfer from the bulk to the support surface. This enhanced oxygen mobility results in more Ce^{3+} species and oxygen vacancies [31]. In a similar Ca-doped CeO_2 oxide, Ce^{3+} surface enrichment was obtained by both Ca ↔ O ↔ Ce interactions and O vacancies [32]. Recently, the enrichment of Ce^{3+} by Pd doping has also been reported for a Pd/$MnCeO_x$ sample, contributing to the interaction between Pd and CeO_2 [21]. Thus, the higher abundance of Ce^{3+} in amorphous samples indicates more oxygen vacancies and enhanced oxygen mobility.

Fig. 7b shows the experimental and fitted Mn2$p_{3/2}$ spectra of these four samples. Previous XRD, TEM, and TPR results indicated the coexistence of different manganese oxides. The peaks around 642.2 and 640.9 eV are attributed to the presence of Mn^{4+} and Mn^{3+} species, respectively. Surprisingly, Mn^{2+} is undetectable in the fitted spectra, probably because Mn^{2+} may be partially incorporated into the fluorite structure of CeO_2 by isomorphous substitution [33]. Since only the outmost layers can be detected by XPS, this results in a higher oxidation state of Mn on the surface than in the bulk. The unobvious peak at around 645.0 eV originates from charge transfer between the outer electron shell of the ligand and the unfilled 3*d* shell of Mn during the creation of the core–hole in the photoelectron process [26]. Mn^{4+} is the dominant species in 7Mn3Ce-A, whereas the amount of Mn^{3+} becomes considerable in 7Mn3Ce-C. Moreover, the main Mn2$p_{3/2}$ component of 7Mn3Ce-C possesses a lower BE than 7Mn3Ce-A, indicating that more electrons are transferred from Ce to Mn during co-precipitation. Deposition of Pd slightly decreases the oxidation state of surface manganese species, and the feature assigned to Mn^{3+} is discernable in Pd/7Mn3Ce-A, which may be due to the partial reduction of Mn species during MAPR synthesis. Pd/7Mn3Ce-A exhibits a higher Mn BE than Pd/7Mn3Ce-C, implying that a large

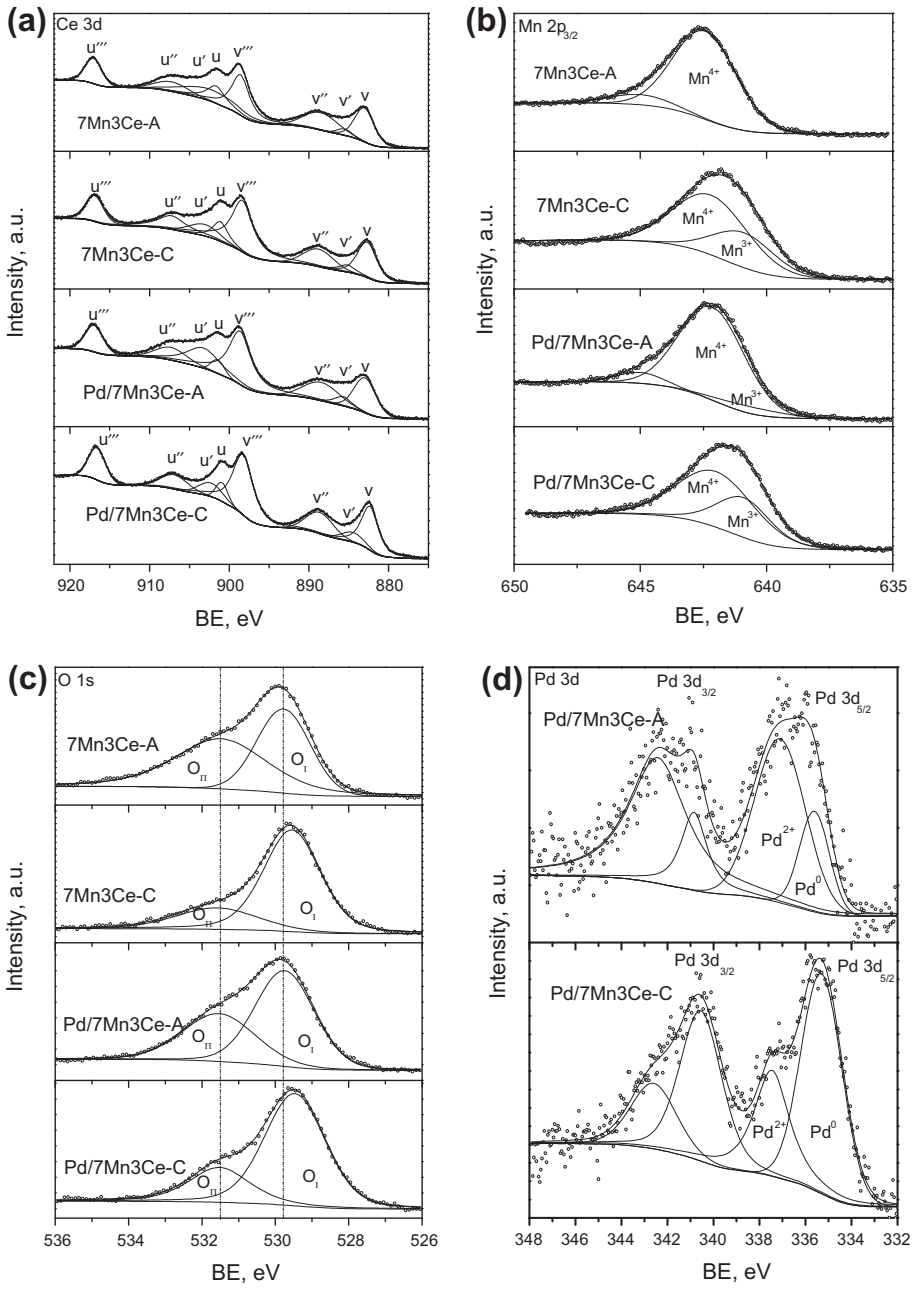

Fig. 7. XPS results of representative $MnCeO_x$ samples: (a) Ce3*d*; (b) Mn2*p*; (c) O1*s*; (d) Pd3*d*.

amount of Mn^{4+} species exists on the support surface. These changes are quantitatively reflected in Table 3. The relative surface concentration of Mn^{4+} in 7Mn3Ce-A is 100%, while only 67.14% is detected in 7Mn3Ce-C. After Pd deposition, Mn^{4+} concentration declines slightly to 93.04% and 64.99% in Pd/7Mn3Ce-A and Pd/7Mn3Ce-C, respectively. Correspondingly, the AON (average oxidation number) value *x* in MnO_x decreases from 2.05 for 7Mn3Ce-A to 2.00 for Pd/7Mn3Ce-A, while it decreases from 1.84 for 7Mn3Ce-C to 1.82 for Pd/7Mn3Ce-C.

The quantitative deconvolution of the O1*s* core-level spectra for all samples seems to be difficult, due to the large number of oxygen species related to various cerium and manganese oxides, as well as the presence of surface oxygen species such as carbonate and hydroxyl groups. Particularly, the O1*s* BE for CeO_2 may shift from 529.6 to 530.3 eV, therefore overlapping with those of various MnO_x oxides ranging from 529.3 to 530.0 eV [1]. Hence, no attempt was made to analyze these components individually, and the O1*s* spectra were fitted using only two main features (Fig. 7c): (i) the low BE component O_I assigned to the lattice oxygen (O^{2-}), and (ii) the high BE component O_{II} ascribed to other surface oxygen species (e.g., chemisorbed oxygen O_2^- and O^-) [13]. The amorphous samples possess a higher BE of the O_I component (529.8 eV) than the crystalline ones (529.5 eV), indicating that an "Mn ← O" electron transfer occurs in $MnCeO_x$ with high dispersion [15]. The relative abundance of these two oxygen components is reported in Table 3. 7Mn3Ce-A has a 55.44% O_{II} component, which is nearly twice the amount in 7Mn3Ce-C. After Pd deposition, Pd/7Mn3Ce-A still has more O_{II} component than Pd/7Mn3Ce-C, though the difference is slightly smaller. The formation of the O_{II} component is closely related to the nature of the $MnCeO_x$ support. Mn–O–Ce bonds, which are formed at Mn–Ce boundary by partial incorporation of Mn ions into the cubic CeO_2 structure, enhance the

Table 3
Surface compositions calculated from XPS results of representative samples.

Entry	Sample	Surface atoms percentage (%)				Surface Mn/Ce ratio	Relative abundance of Ce^{3+} and Ce^{4+} (%)		Relative abundance of Mn^{4+} and Mn^{3+} (%)			Relative abundance of O_I and O_{II}/%		Relative abundance of Pd^0 and Pd^{2+}/%	
		Mn	Ce	O	Pd		Ce^{3+}	Ce^{4+}	Mn^{4+}	Mn^{3+}	AON of Mn	O_I	O_{II}	Pd^0	Pd^{2+}
1	7Mn3Ce-A	21.80	10.25	67.95	0	2.13	34.57	65.43	100	0	2.05	44.56	55.44	–	–
2	7Mn3Ce-C	17.61	8.97	73.42	0	1.96	19.17	80.83	67.14	32.86	1.84	76.96	23.04	–	–
3	Pd/7Mn3Ce-A	17.81	8.15	73.73	0.31	2.19	43.46	56.54	93.04	6.96	2.00	61.69	38.31	26.49	73.51
4	Pd/7Mn3Ce-C	13.97	8.06	77.49	0.48	1.73	21.59	78.41	64.99	35.01	1.82	74.41	25.59	63.91	36.09

formation of oxide defects. Therefore, a large number of oxygen vacancies on the surfaces of CeO_2 and MnO_x species are formed due to a high degree of coordinative unsaturation, as suggested by TPR data. These vacancies act as active sites for molecular oxygen adsorption and activation, forming O_{II} species [34].

The Pd3*d* XPS spectra in Fig. 7d consists of two asymmetric peaks assigned to Pd3$d_{5/2}$ and Pd3$d_{3/2}$ core levels, which can be fitted using two doublets. The peaks around 335.4 and 340.7 eV are attributed to metallic Pd^0m, while those around 337.3 and 342.4 eV correspond to Pd^{2+} species. Despite the existence of both Pd^0 and Pd^{2+} species in both samples, Pd/7Mn3Ce-A possesses a higher abundance of Pd^{2+} than Pd/7Mn3Ce-C (73.51 and 36.09%, respectively). The results discussed earlier have shown that 7Mn3Ce-A exhibits a stronger surface O_{II} component than 7Mn3Ce-C, which indicates a stronger oxidizing ability [1]. Thus, it can be speculated that, during the catalyst synthesis process, this active O_{II} species may be transferred from the support surface to the Pd nanoparticles, resulting in a strong interaction between Pd and $MnCeO_x$ mixed oxides and the generation of Pd^{2+} species. A similar result was reported by Tang et al., indicating that Ag^+ species can be more stable after silver deposition onto MnO_x–CeO_2 support [12]. In addition, Pd^{2+} in both catalysts exhibits higher Pd 3$d_{5/2}$ BEs than PdO (336.8 eV), implying high dispersion and deficient coordination of Pd in intimate contact with $MnCeO_x$ support, as well as subsequent promoted oxygen transfer from the support to Pd active sites [31].

4. Discussion

Our results suggest that, regardless of the structure of $MnCeO_x$ supports (crystalline or amorphous), the catalytic performance (conversion and selectivity) and stability of Pd catalysts can be improved by combining Mn and Ce to form $MnCeO_x$ mixed oxides. This effect is attributed to the strong synergetic interactions among MnO_x, CeO_2, and Pd. However, a significant difference in the catalytic behavior appears when different $MnCeO_x$ support materials are used. Pd/7Mn3Ce-C shows higher activity than Pd7Mn3Ce-A in the initial stage of the reaction, whereas it undergoes a more rapid loss of both conversion and selectivity over a long reaction run (Fig. 1). Based on these characterization results, this different catalytic behavior can be explained by three essential factors: texture and structure, redox properties, and surface composition.

According to the reaction kinetics, the initial reaction rate is defined as $r_0 = -\frac{dC_A}{dt}\Big|_{t=0} = -\frac{dC_{A0}(1-x)}{dt}\Big|_{t=0} = C_{A0}\frac{dx}{dt}\Big|_{t=0}$, where C_{A0} and x are the initial concentration and the conversion of benzyl alcohol, respectively. Thus, the initial rate is directly proportional to the slope of the tangent of the conversion curves at $t = 0$. Fig. 1 shows that Pd/7Mn3Ce-C has a greater slope than Pd/7Mn3Ce-A, i.e., a higher initial reaction rate. The initial reaction rates r_0 are 11.5 and 8.4 mmol/h for Pd/7Mn3Ce-C and Pd/7Mn3Ce-A, respectively. Recently, Abad et al. have proposed a reaction mechanism in which the initial reaction rate of benzyl alcohol oxidation can be represented as $r_0 = kC_{A0}C_{M0}$, where C_{M0} is the initial concentration of metal active sites. Since C_{A0} is constant at the beginning of the reaction for both catalysts, the initial rate should correlate linearly with the concentration of available metal active sites [35]. A large fraction of Pd exposed to the liquid environment results in the high availability of adsorption sites for the reactants, which may account for the high activity in the initial stage of the reaction. Herein, the presence of more Pd active sites accessible to the reactants in Pd/7Mn3Ce-C than in Pd/7Mn3Ce-A, which is confirmed by XPS results, contributes primarily to the higher initial rate. A reasonable explanation can be derived from textural and structural differences of the two supports. The 7Mn3Ce-C support possesses a smaller surface area than the 7Mn3Ce-A support. Nonetheless, the support surface area may not be the most important factor in the catalytic activity, since the Pd loading used in this study is quite low. The enlarged surface area of 7Mn3Ce-A is primarily due to the existence of small crystals of Mn–Ce solid solutions rather than large crystallites of Mn oxides [14]. Therefore, the relatively smaller specific surface area but larger pore diameter of crystalline support than of amorphous support may facilitate the anchoring and deposition of Pd active species onto the support surfaces during the catalyst synthesis, as well as the transport of reactants during the reaction. In contrast, the inferior framework of amorphous $MnCeO_x$ may lead to the Pd nanoparticles embedded in the matrix, suppressing contact between Pd active sites and reactants.

Previous results demonstrate that Pd acts as the sole active element and both Pd^0 and Pd^{2+} species exist on crystalline and amorphous $MnCeO_x$-supported Pd catalysts. To eliminate the effect of Pd content and investigate the relationship between catalytic activity and the nature of active species, the specific initial rate is introduced here: $r_{s0} = \frac{r_0}{pd\ content}$. Here, Pd/7Mn3Ce-C possesses a higher r_{s0} than Pd/7Mn3Ce-A (151,316 and 110,526 mmol/g_{Pd} · h, respectively). From XPS results, Pd7Mn3Ce-C contains more surface Pd^0 species than Pd/7Mn3Ce-A, indicating that the initial reaction rate is higher when the relative amount of Pd^0/Pd^{2+} is greater. This is in good agreement with the proposal that metallic Pd^0 is more active than palladium oxide in the aerobic oxidation of benzyl alcohol [36,37]. In benzyl alcohol oxidation over Pd/Al_2O_3 catalysts, Pd is in the reduced state (Pd^0) even in the presence of oxygen, which is attributed to the strong reducing character of benzyl alcohol [38]. Our previous study also showed that a Pd catalyst supported on CNT consists only of metallic Pd^0 species after reaction [39]. Thus, metallic Pd^0 is responsible for the high catalytic activity. When Pd^{2+} is the primary component, a long induction period was essential to transform the supported Pd^{2+} species to metallic Pd nanoparticles, the true active species [40]. Here, Pd/7Mn3Ce-A consists of larger amounts of Pd^{2+} than of Pd^0, exhibiting a low initial catalytic activity. Therefore, it can be concluded that the initial reaction activity is intimately related to the accessibility of exposed Pd active sites and the surface Pd^0 concentration.

Despite a low initial reaction activity, Pd/7Mn3Ce-A shows enhanced catalyst stability and resistance against deactivation, which can be observed from the redox properties and the surface composition of the support. The support does not directly influence the dehydrogenation step but affects the adsorption, activation, and transfer of oxygen, which also has a strong effect on the activity. Previous characterization results have shown that 7Mn3Ce-A support possesses a higher abundance of oxygen vacancies and surface O_{II} species (chemisorbed oxygen O_2^- and O^-). O_{II} species have stronger oxidizing ability and higher mobility, which contribute to the enhanced oxygen transfer and redox cycle via easy transformation of the lattice oxygen O^{2-} due to abundant oxygen vacancies accompanied by the formation of Ce^{3+} species [1]. During the oxygen transfer, these short-lived but highly active chemisorbed oxygen species, O_2^- and O^-, can be activated rapidly by diffusing into the CeO_2 lattice vicinity and being converted into lattice oxygen O^{2-} [41]. Due to the high oxygen mobility in the 7Mn3Ce-A support, the vacancies around Pd nanoparticles after the lattice oxygen O^{2-} is consumed are rapidly replenished by oxygen spillover from the bulk of the support, and the oxygen distribution on the surface is equilibrated. On the other hand, the replenishment of oxygen in the 7Mn3Ce-C support, which has lower oxygen mobility and fewer oxygen vacancies, mainly comes from the gas phase. Under such an insufficient oxygen supply, Pd active sites would be covered with hydrogen and carbonaceous deposits and deactivated, leaving only the sites for decarbonylation still active [42]. Thus, the generation of benzaldehyde would be suppressed and the decomposition and further oxidation of the carbonyl product would take place, leading to lower activity and selectivity over the Pd/7Mn3Ce-C catalyst. The presence of more oxygen vacancies and surface O_{II} species in the amorphous support, as well as more Mn ions in a high oxidation state (Mn^{4+}), also contributes significantly to the oxygen transfer. In contrast to the Ce surface enrichment and the remarkably low surface dispersion of Mn in crystalline $MnCeO_x$ samples, amorphous $MnCeO_x$ support materials exhibit a homogeneous dispersion of Mn^{4+} and Ce^{4+} ions [26]. Mn species in higher oxidation states can facilitate the redox cycles and improve the oxygen mobility and availability, resulting in enhanced catalytic activity [1,8,43]. Moreover, the enhanced redox properties exhibited by $MnCeO_x$ can promote the reversible sorption/desorption cycles of lattice oxygen [28]. Therefore, the mutual promotion between redox properties and oxygen mobility leads to enhanced catalyst stability and lower deactivation in the selective oxidation of benzyl alcohol [16].

Catalytic results show that Pd/$MnCeO_x$ catalyst can effectively suppress the formation of toluene, giving high benzaldehyde selectivity. To clarify the origin of toluene formation and the mechanism of benzyl alcohol oxidation, catalytic tests were conducted in N_2 over Pd/7Mn3Ce-C and Pd/7Mn3Ce-A catalysts. Under such anaerobic conditions, both catalysts exhibit catalytic activities of 0.9% conversion (Table 1, entries 12 and 13), implying the existence of a dehydrogenation mechanism in which benzaldehyde formation occurs in the absence of oxygen. Benzyl alcohol is mainly converted to benzaldehyde (toluene selectivities are 2.1% and 1% for Pd/7Mn3Ce-C and Pd/7Mn3Ce-A, respectively). The formation of toluene is rather complex and has been extensively investigated. Besides the hydrogenolysis of benzyl alcohol [38], toluene can also originate from the disproportionation of benzyl alcohol, yielding an equimolar mixture of benzaldehyde and toluene [44–46]. Moreover, Jayamani et al. also demonstrated that toluene can be formed by the decomposition of dibenzyl ether [47]. Since no ether is detected in the present study, this route can be ruled out. Therefore, the negligible production of toluene under anaerobic conditions clearly suggests that toluene is formed by hydrogenolysis of benzyl alcohol rather than by disproportionation, and benzyl alcohol oxidation follows most likely a dehydrogenation mechanism.

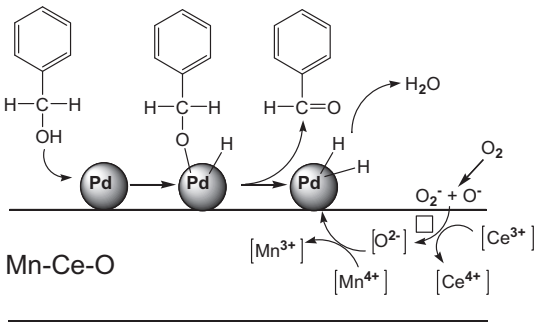

Scheme 1. Overall reaction mechanism for benzyl alcohol oxidation over Pd/$MnCeO_x$ catalysts.

Based on the conventional dehydrogenation mechanism, an integrated alcohol oxidation mechanism over Pd/$MnCeO_x$ is proposed (Scheme 1). In this mechanism, Pd acts as the sole catalytic center where the reaction takes place, and the oxygen transfer is completed through the support via a redox cycle. Benzyl alcohol is adsorbed onto Pd nanoparticles, forming a metal–alkoxide intermediate and adsorbed hydrogen via O–H bond cleavage. Then it is further converted to benzaldehyde through β-hydrogen elimination as the rate-limiting step, leaving reduced Pd sites partially covered by hydrogen, i.e., Pd-hydride. The adsorbed oxygen on the support surface dissociates into chemisorbed oxygen species O_2^- and O^-, diffuses into the support lattice vicinity, and subsequently is activated at the oxygen vacancies and converted into lattice oxygen O^{2-}, accompanied by the transformation of Ce^{3+} to Ce^{4+}. The lattice oxygen is further transferred through the oxide defects in $MnCeO_x$ supports and migrates to the interface between the support and Pd active sites. Finally, it reacts with Pd-hydride to regenerate Pd active sites, forming H_2O as product. The poor catalytic activity over a mixture of Pd/CeO_2 and Pd/MnO_x catalysts (entry 11, Table 1) verifies that this oxygen migration can be facilitated only over $MnCeO_x$ mixed oxides rather than over the physical mixture. The dehydrogenation–oxidation of benzyl alcohol is completed via a synergetic redox cycle and electron transfer involving Pd, Mn, and Ce: Pd ↔ Mn ↔ Ce. A similar consecutive oxygen transfer mechanism was also proposed in a Ag/MnO_x–CeO_2 system, in which oxygen is transferred from the oxygen reservoir of CeO_2 to activate Ag_2O sites through MnO_x [12]. Consequently, the synergetic interactions among Pd, MnO_x, and CeO_2 are enhanced due to the mutual promotion of texture and structure, redox properties, and surface composition, leading to improved catalytic activity and higher resistance against deactivation.

5. Conclusions

Both crystalline and amorphous $MnCeO_x$ supports were successfully synthesized by co-precipitation and redox precipitation methods, respectively. Pd was subsequently deposited by an easy MAPR procedure, leading to the formation of highly dispersed Pd nanoclusters. $MnCeO_x$ supports remarkably enhanced both the catalytic activity and the selectivity in the aerobic oxidation of benzyl alcohol, compared with the single MnO_x and CeO_2 oxides. The highest qTOFs were achieved over Pd/7Mn3Ce-C (15,235 h^{-1}) and Pd/7Mn3Ce-A (14,438 h^{-1}), and the activity can be maintained over five consecutive reaction runs. Pd acts as the sole active component, and the enhanced catalytic activity can be attributed to synergetic interactions among Pd, MnO_x, and CeO_2. Good accessibility of Pd active sites and high concentration of surface Pd^0 contribute to the high initial reaction rate over crystalline $MnCeO_x$-supported Pd catalysts. Amorphous $MnCeO_x$-supported Pd catalysts exhibit enhanced catalyst

stability and lower deactivation due to mutual promotion between redox properties and oxygen mobility.

Acknowledgment

Funding from the Singapore Agency for Science, Technology and Research (A*STAR), SERC Grant 102 101 0020, in support of this project is gratefully acknowledged.

Appendix A. Supplementary data

Supplementary data associated with this article can be found, in the online version, at doi:10.1016/j.jcat.2011.06.021.

References

[1] H. Chen, A. Sayari, A. Adnot, F. Larachi, Appl. Catal. B 32 (2001) 195.
[2] Z.Y. Ding, L.X. Li, D. Wade, E.F. Gloyna, Ind. Eng. Chem. Res. 37 (1998) 1707.
[3] S. Aki, M.A. Abraham, Ind. Eng. Chem. Res. 38 (1999) 358.
[4] D. Delimaris, T. Ioannides, Appl. Catal. B 84 (2008) 303.
[5] H. Li, X.L. Tang, H.H. Yi, L.L. Yu, J. Rare Earth 28 (2010) 64.
[6] G.S. Qi, R.T. Yang, J. Catal. 217 (2003) 434.
[7] F. Arena, G. Trunfio, J. Negro, L. Spadaro, Mater. Res. Bull. 43 (2008) 539.
[8] X.F. Tang, Y.G. Li, X.M. Huang, Y.D. Xu, H.Q. Zhu, J.G. Wang, W.J. Shen, Appl. Catal. B 62 (2006) 265.
[9] A. Trovarelli, Catal. Rev. Sci. Eng. 38 (1996) 439.
[10] F. Arena, G. Trunfio, J. Negro, L. Spadaro, Appl. Catal. B 85 (2008) 40.
[11] F. Eigenmann, M. Maciejewski, A. Baiker, Appl. Catal. B 62 (2006) 311.
[12] X.F. Tang, J.L. Chen, Y.G. Li, Y. Li, Y.D. Xu, W.J. Shen, Chem. Eng. J. 118 (2006) 119.
[13] F. Arena, G. Trunfio, B. Fazio, J. Negro, L. Spadaro, J. Phys. Chem. C 113 (2009) 2822.
[14] G. Blanco, M.A. Cauqui, J.J. Delgado, A. Galtayries, J.A. Perez-Omil, J.M. Rodriguez-Izquierdo, Surf. Interface Anal. 36 (2004) 752.
[15] F. Arena, G. Trunfio, J. Negro, B. Fazio, L. Spadaro, Chem. Mater. 19 (2007) 2269.
[16] Q.H. Tang, C.M. Wu, X.O. Huang, Y.H. Yang, Chin. J. Catal. 30 (2009) 207.
[17] A.F.J. Santiago, J.F. Sousa, R.C. Guedes, C.E.M. Jeronimo, M. Benachour, J. Hazard. Mater. 138 (2006) 325.
[18] S. Hamoudi, A. Sayari, K. Belkacemi, L. Bonneviot, F. Larachi, Catal. Today 62 (2000) 379.
[19] M.P. Checinski, A. Bruckner, J. Radnik, A. Kockritz, Appl. Catal. A 366 (2009) 212.
[20] T. Sato, T. Komanoya, Catal. Commun. 10 (2009) 1095.
[21] Z.Q. Zou, M. Meng, Y.Q. Zha, J. Phys. Chem. C 114 (2010) 468.
[22] Z. Guo, Y. Chen, L. Li, X. Wang, G.L. Haller, Y. Yang, J. Catal. (2010).
[23] E.P. Barrett, L.G. Joyner, P.P. Halenda, J. Am. Chem. Soc. 73 (1951) 373.
[24] S. Brunauer, P.H. Emmett, E. Teller, J. Am. Chem. Soc. 60 (1938) 309.
[25] H.P. Klug, L.E. Alexander, X-Ray Diffraction Procedures for Polycrystalline and Amorphous Materials, second ed., John Wiley, New York, 1974.
[26] Y.S. Wu, Y.X. Zhang, M. Liu, Z.C.C. Ma, Catal. Today 153 (2010) 170.
[27] L.M. Shi, W. Chu, F.F. Qu, J.Y. Hu, M.M. Li, J. Rare Earth 26 (2008) 836.
[28] M. Machida, M. Uto, D. Kurogi, T. Kijima, Chem. Mater. 12 (2000) 3158.
[29] J.A. Perez-Omil, J.J. Delgado, W. Ouahbi, A.B. Hungria, N. Browning, M.A. Cauqui, J.M. Rodriguez-Izquierdo, J.J. Calvino, J. Phys. Chem. C 114 (2010) 8981.
[30] F. Kapteijn, L. Singoredjo, A. Andreini, J.A. Moulijn, Appl. Catal. B 3 (1994) 173.
[31] L.H. Xiao, K.P. Sun, X.L. Xu, Acta Phys. Chim. Sin. 24 (2008) 2108.
[32] J.A. Rodriguez, X.Q. Wang, J.C. Hanson, G. Liu, A. Iglesias-Juez, M. Fernandez-Garcia, J. Chem. Phys. 119 (2003) 5659.
[33] W.-J. Hong, S. Iwamoto, S. Hosokawa, K. Wada, H. Kanai, M. Inoue, J. Catal. 277 (2011) 208.
[34] S. Imamura, Y. Okumura, T. Nishio, K. Utani, Y. Matsumura, Ind. Eng. Chem. Res. 37 (1998) 1136.
[35] A. Abad, A. Corma, H. Garcia, Chem. Eur. J. 14 (2008) 212.
[36] J.D. Grunwaldt, M. Caravati, A. Baiker, J. Phys. Chem. B 110 (2006) 25586.
[37] C. Mondelli, D. Ferri, J.D. Grunwaldt, F. Krumeich, S. Mangold, R. Psaro, A. Baiker, J. Catal. 252 (2007) 77.
[38] C. Keresszegi, D. Ferri, T. Mallat, A. Baiker, J. Phys. Chem. B 109 (2005) 958.
[39] Y. Chen, L. Bai, C. Zhou, J.-M. Lee, Y. Yang, Chem. Commun. (2011), doi:10.1039/c1cc11643f.
[40] K. Mori, T. Hara, T. Mizugaki, K. Ebitani, K. Kaneda, J. Am. Chem. Soc. 126 (2004) 10657.
[41] C. Bozo, N. Guilhaume, J.-M. Herrmann, J. Catal. 203 (2001) 393.
[42] C. Keresszegi, D. Ferri, T. Mallat, A. Baiker, J. Catal. 234 (2005) 64.
[43] F. Arena, J. Negro, A. Parmaliana, L. Spadaro, G. Trunfio, Ind. Eng. Chem. Res. 46 (2007) 6724.
[44] S. Meenakshisundaram, E. Nowicka, P.J. Miedziak, G.L. Brett, R.L. Jenkins, N. Dimitratos, S.H. Taylor, D.W. Knight, D. Bethell, G.J. Hutchings, Faraday Discuss. 145 (2010) 341.
[45] G. Kovtun, T. Kameneva, S. Hladyi, M. Starchevsky, Y. Pazdersky, I. Stolarov, M. Vargaftik, I. Moiseev, Adv. Syn. Catal. 344 (2002) 957.
[46] S.S. Hladyi, M.K. Starchevsky, Y.A. Pazdersky, M.N. Vargaftik, I. Moiseev I and II, Mendeleev Commun. (2002) 45.
[47] M. Jayamani, C.N. Pillai, J. Catal. 82 (1983) 485.